The Astrophysical Journal, 816:5 (8pp), 2016 January 1 doi:10.3847/0004-637X/816/1/5


# HORIZONTAL FLOWS IN ACTIVE REGIONS FROM RING-DIAGRAM AND LOCAL CORRELATION TRACKING METHODS

Kiran Jain[1], S. C. Tripathy[1], B. Ravindra[2], R. Komm[1], and F. Hill[1]
[1] National Solar Observatory, 950 N Cherry Avenue, Tucson, AZ 85719, USA; kjain@nso.edu
[2] Indian Institute of Astrophysics, Block 2, Koramangala, Bangaluru, 560034, India
*Received 2015 October 1; accepted 2015 November 7; published 2015 December 21*

## ABSTRACT

Continuous high-cadence and high spatial resolution Dopplergrams allow us to study subsurface dynamics that may be further extended to explore precursors of visible solar activity on the surface. Since the *p*-mode power is absorbed in the regions of high magnetic field, the inferences in these regions are often presumed to have large uncertainties. In this paper, using the Dopplergrams from space-borne Helioseismic Magnetic Imager, we compare horizontal flows in a shear layer below the surface and the photospheric layer in and around active regions. The photospheric flows are calculated using the local correlation tracking (LCT) method, while the ring-diagram technique of helioseismology is used to infer flows in the subphotospheric shear layer. We find a strong positive correlation between flows from both methods near the surface. This implies that despite the absorption of acoustic power in the regions of strong magnetic field, the flows inferred from the helioseismology are comparable to those from the surface measurements. However, the magnitudes are significantly different; the flows from the LCT method are smaller by a factor of 2 than the helioseismic measurements. Also, the median difference between the direction of corresponding vectors is 49°.

*Key words:* Sun: helioseismology – Sun: interior – Sun: magnetic fields – Sun: photosphere

## 1. INTRODUCTION

The dynamic nature of the Sun is manifested by eruptions observed in different layers of the solar atmosphere. These eruptions generally originate from regions that harbor strong magnetic fields. Propagating acoustic waves interact with these regions and modify their properties. It is believed that the presence of a high magnetic field affects the equilibrium profile of sound speed and density in the solar interior, which further modifies the characteristics of acoustic oscillations. As a result, while oscillation frequencies vary in phase with the solar activity cycle (e.g., Jain et al. 2009), the acoustic power is anticorrelated (Rajaguru et al. 2001; Jain et al. 2008). The availability of high spatial resolution continuous Doppler images in the past two decades has opened a new dimension in the field of helioseismology where properties of active regions below the solar surface are being explored in detail. However, these studies are often subjected to the uncertainties in inferred properties, such as subsurface structure and flows, due to the absorption of acoustic power.

The subsurface flows in active regions are estimated using the techniques of local helioseismology. These techniques are capable of probing the solar interior in three dimensions (Antia & Basu 2007) and allow us to infer flows in different layers from the surface to several megameters in depth, which have become a crucial ingredient in computing solar dynamo models. While the ring-diagram method (RD; Hill 1988) provides flows in shallow layers (e.g., González Hernández et al. 2006; Jain et al. 2012, 2015; Komm et al. 2015), the time–distance method (TD; Duvall et al. 1993) is capable of providing flows in much deeper layers (e.g., Zhao et al. 2013; Kholikov & Hill 2014). A detailed comparison between the horizontal flows obtained from these two methods was carried out by Hindman et al. (2004) using data from 2 yr of the Michelson Doppler Imager Dynamics Program. These authors found a good agreement between flows obtained from RD and TD methods.

On the other hand, efforts have also been made to validate flows near the surface from helioseismology by directly comparing with surface measurements, mainly with feature tracking methods. Švanda et al. (2007) compared the flows obtained from TD and local correlation tracking (LCT; November & Simon 1988) methods and reported a significantly high correlation; however, the magnitudes from both methods were significantly different. They suggested that the measurements from TD were correct and the magnitude of the LCT measurements must be corrected. Measurements from the TD and LCT methods were also compared with the realistic simulations of solar convection by Georgobiani et al. (2007), who found similar large-scale convective patterns. This study was primarily confined to using the *f*-mode ridge. Later, Zhao et al. (2007) validated the TD method by computing acoustic travel times and inferring mean flow fields using a ray-approximation-based inversion for different depths of the simulated data of Georgobiani et al. (2007). More studies were carried out recently using the Helioseismic and Magnetic Imager (HMI) observations to verify helioseismic methods (Liu et al. 2013; Švanda et al. 2013); however, none were focused on validating flows from the RD method. In all these studies, strong positive correlations were obtained for both zonal and meridional components. In addition, Liu et al. (2013) have also identified the areas where the angle between the flows from TD and DAVE4VM was greater than 90°, i.e., the flows point in different directions. Most of these areas were either inside the sunspot penumbra or far away from the sunspot, where the DAVE4VM becomes insensitive owing to the weak magnetic field strength. In this paper, we present results on the horizontal flow measurements from RD and LCT methods with several aims: (i) validation of horizontal flows from inversion in the RD method, (ii) how different/similar are the flows from helioseismic and surface measurements, (iii) identifying areas where both methods diverge or converge, and (iv) determining

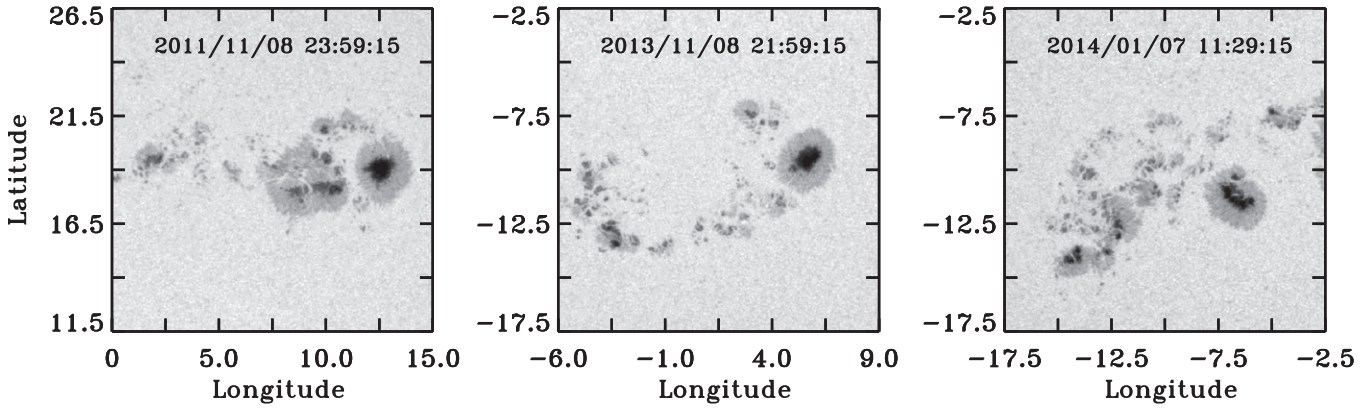


**Figure 1.** HMI Continuum images of three active regions used in this study: AR 11339 (left), AR 11890 (middle), and AR 11944 (right).

**Table 1**
Details of Data Used in This Study

| Active Region | | | Time Series | | Duty | Location[c] | |
|---|---|---|---|---|---|---|---|
| Number | Type[a] | Area[b] | Start | End | Cycle | Longitude | Latitude |
| NOAA 11339 | $\beta\gamma$ | 940 | 2011 Nov 08 12:00:00 UT | 2011 Nov 09 11:59:15 UT | 99.84% | 7.°5 | 19.°0 |
| NOAA 11890 | $\beta\gamma\delta$ | 920 | 2013 Nov 08 10:00:00 UT | 2013 Nov 09 09:59:15 UT | 99.95% | 1.°5 | −10.°0 |
| NOAA 11944 | $\beta\gamma\delta$ | 1540 | 2014 Jan 06 23:30:00 UT | 2014 Jan 07 23:29:15 UT | 99.63% | −10.°0 | −9.°5 |

**Notes.**
[a] Magnetic configuration of the spots in the Mt. Wilson system.
[b] Area of spots in millionths of the visible hemisphere.
[c] The locations are listed for the central pixel of the reference image in a 15° × 15° tile.

whether the helioseismic measurements provide reliable estimates of flows in the regions of high magnetic field.

The paper is organized as follows: the selection of data and the methods to derive horizontal flows are described in Section 2. In Section 3, we discuss and compare results obtained from different methods. Finally, the findings of this study are summarized in Section 4.

## 2. SELECTION OF DATA AND ESTIMATION OF FLOWS

We select three active regions from the current solar cycle, NOAA 11339, 11890, and 11944, and use 45 s cadence continuous high spatial resolution full-disk Dopplergrams from the HMI (Scherrer et al. 2012) on board *Solar Dynamics Observatory* (*SDO*; Pesnell et al. 2012) to calculate flows in the regions of high magnetic field. Images of all three active regions in the HMI continuum are shown in Figure 1.

To calculate flows in each active region, we first choose an area of 15° × 15° surrounding the active region near disk center and track for 1440 minutes using the surface rotation rate (Snodgrass 1984). Start and end times of each time series are provided in Table 1. The spatial sampling of the HMI Dopplergrams is 0.″5; thus, regions of 384 × 384 pixels were selected. We use the same tracked data cubes to determine flows in both photospheric and subphotospheric shear layers. The active regions analyzed here are well developed and moderately large, with a significant number of sunspots with a spread of about 13°–18° in longitude. AR 11139 and AR 11890 have similar characteristics with low flaring activity, while AR 11944 is much bigger in size and produced X1.1 and M7.2 class flares, in addition to five C-class flares during the period of analysis. Since gaps in time series introduce uncertainties in flow estimation, the time series have been cautiously chosen when the duty cycle is ≈100% and the active regions are located near disk center to avoid any influence of systematics in flow determination. Duty cycle and the location of the reference image for each time series are given in Table 1.

### 2.1. Photospheric Flows

Photospheric flows are calculated using the technique of LCT. This method has been widely used to infer photospheric motion in active regions/sunspots (Ravindra et al. 2008, and references therein). In this method, the local velocity in an image is estimated from the displacement of a feature between two consecutive images $I(x, t)$ and $I(x, t + \Delta t)$, where $I(x, t)$ represents the reference image as a function of position $x$ and time $t$, and the displacement is calculated by cross-correlating pairs of subimages separated by a uniform time interval $\Delta t$.

Here we choose the object image and reference image that are separated by a 4.5-minute interval using a 6.″3 Gaussian apodizing window function. The corresponding velocities in zonal ($x$) and meridional ($y$) directions are computed by dividing the displacements by time difference between the two images. Finally, the velocity at each pixel is averaged over 1440 minutes to determine the long-lived flows in and around active regions.

### 2.2. Subphotospheric Flows

Subphotospheric flows are calculated using the technique of RD. In this method, high-degree waves propagating in

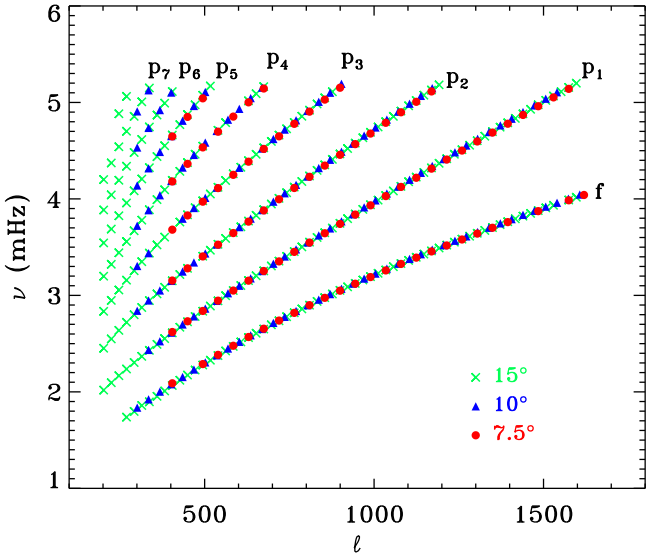


**Figure 2.** Typical $\ell$–$\nu$ diagram of the fitted modes at the disk center for different tile sizes using HMI Dopplergrams. Regions have been tracked for 1440 minutes on 2013 December 15.

localized areas over the solar surface are used to obtain an averaged velocity vector in the region of interest. It has been extensively applied to infer subsurface properties up to a limited depth. Despite its substantial applications, the RD method suffers from the restriction on size of the tiles that restricts the number of fitted modes and the depth range covered in the inversion. As an example, a typical $\ell$–$\nu$ diagram exhibiting fitted modes in three different tile sizes using the HMI Dopplergrams is shown in Figure 2. It can be seen that the number of fitted modes decreases with decreasing tile size. Since a higher value of $\nu/\ell$ denotes the penetration of the traveling waves at greater depth, the smaller tile selection provides reliable results closer to the surface.

Each tracked area is apodized with a circular function, and then a three-dimensional fast Fourier transform is applied on both spatial and temporal direction to obtain a three-dimensional power spectrum. In this study, the corresponding power spectrum is fitted using a Lorentzian profile model (Haber et al. 2000)

$$P(k_x, k_y, \omega) = \frac{A}{\left(\omega - \omega_0 + k_x V x_{\rm Fit} + k_y V y_{\rm Fit}\right)^2 + \Gamma^2} + \frac{b}{k^3}, \quad (1)$$

where $P$ is the oscillation power for a wave with a temporal frequency ($\omega$) and the total wavenumber $k^2 = k_x^2 + k_y^2$. There are six parameters to be fitted: two Doppler shifts ($k_x V x_{\rm Fit}$ and $k_y V y_{\rm Fit}$) for waves propagating in the orthogonal zonal and

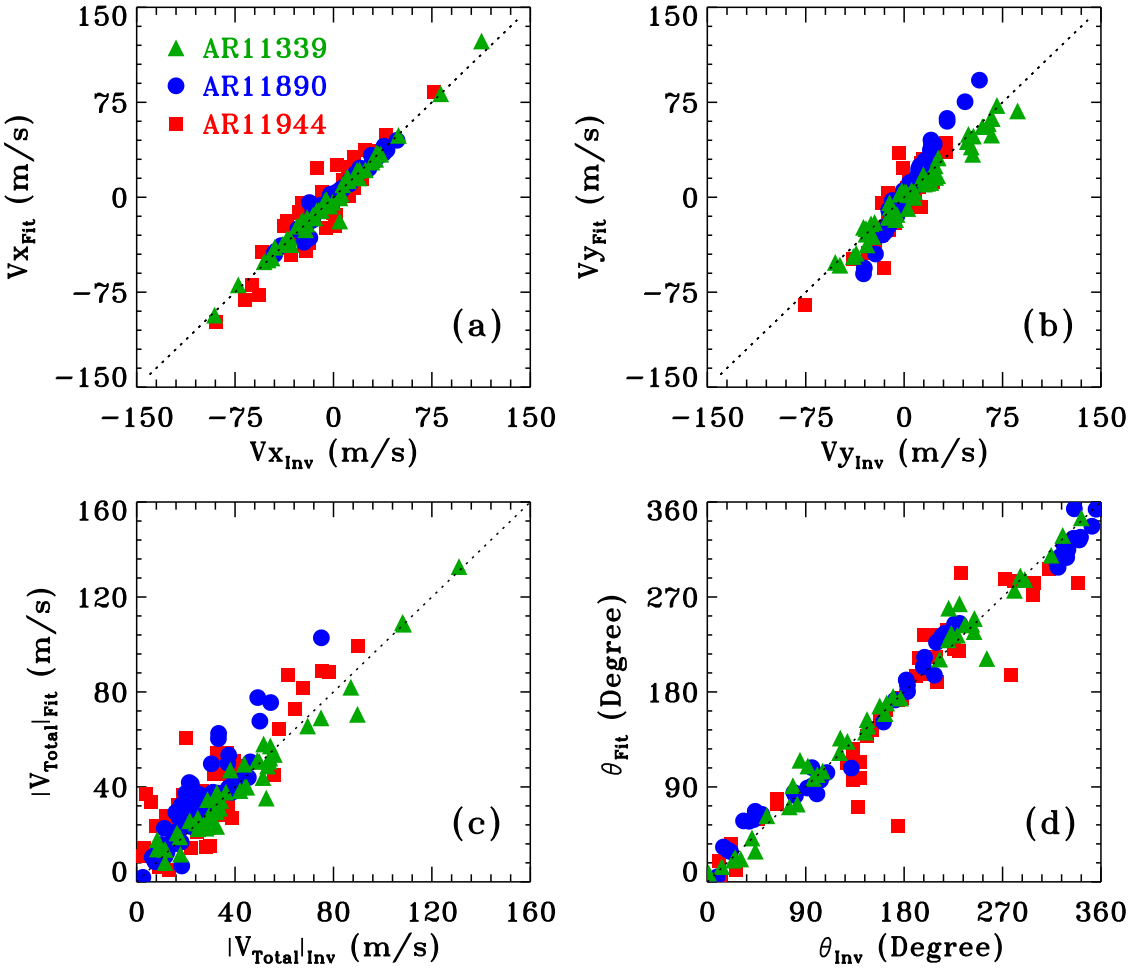


**Figure 3.** Comparison of various quantities calculated using two approaches of ring-diagram analysis: (a) zonal component, (b) meridional component, (c) total magnitude, and (d) azimuthal angle of the horizontal velocity. Values obtained from the inversion are plotted on the $x$-axis, and those from the fitting are on the $y$-axis. The dotted line in each panel corresponds to the ideal scenario where both approaches yield the same results. Statistical uncertainties in velocity estimation are smaller than the size of symbols.

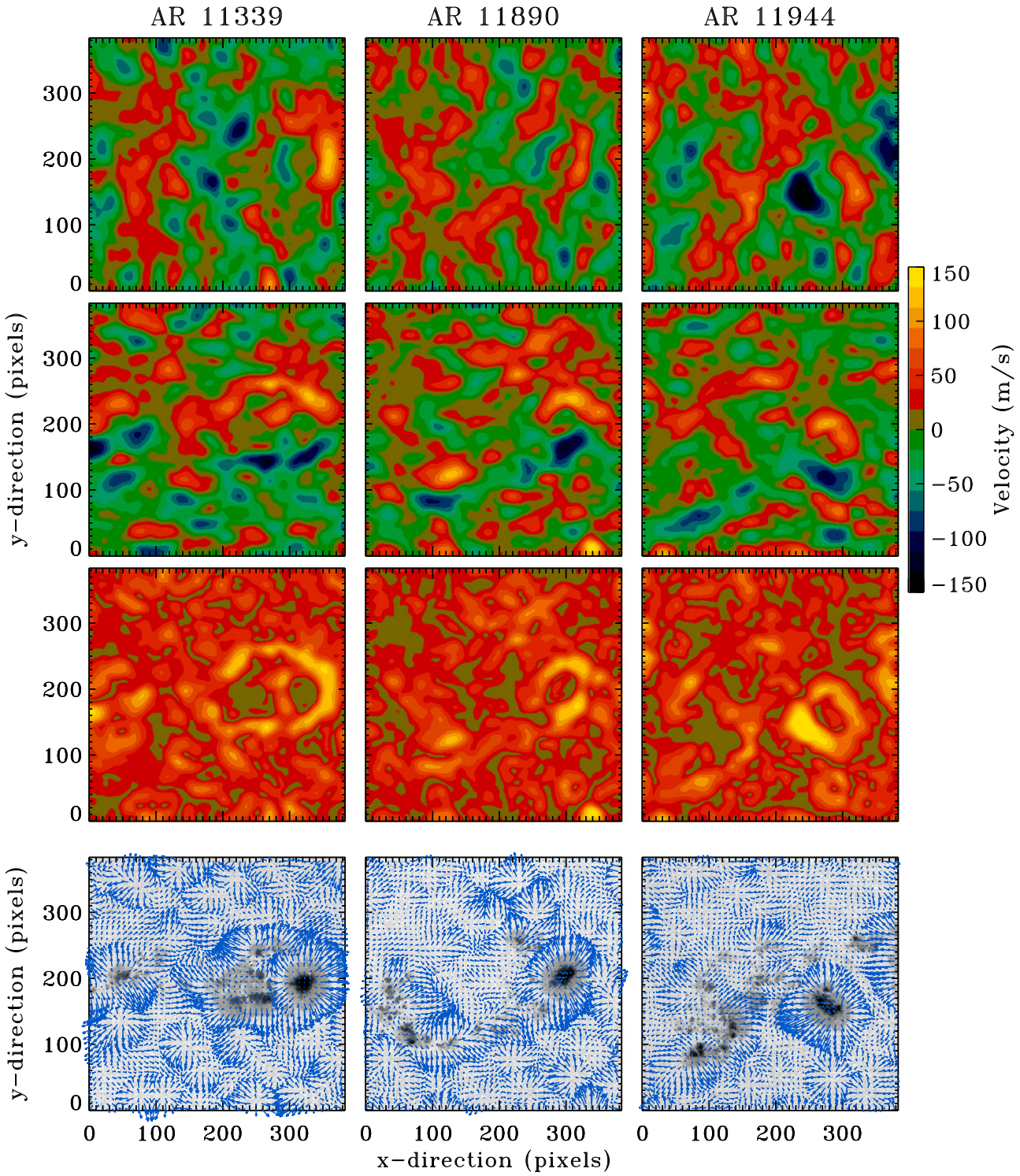


**Figure 4.** Maps of photospheric zonal flow (top row), meridional flow (second row), total horizontal flow (third row), and flow vectors overplotted on the HMI continuum image (bottom row), from the LCT method for three active regions: AR 11339 (left), AR 11890 (middle), and AR 11944 (right). The positive/negative values are for west/east zonal flows and north/south meridional flows. Background images in the bottom row are the same as in Figure 1.

meridional directions, the background power ($b$), the mode central frequency ($\omega_0$), the mode width ($\Gamma$), and the amplitude ($A$). Finally, the fitted velocities ($Vx_{\rm Fit}$ and $Vy_{\rm Fit}$) are inverted using a regularized least-squares (RLS) method to estimate depth dependence of various components of the horizontal velocity ($Vx_{\rm Inv}$ and $Vy_{\rm Inv}$).

In this paper, we divide the tracked region of $15^\circ \times 15^\circ$ into a mosaic of overlapping tiles where each tile is approximately $7.^\circ5 \times 7.^\circ5$ in size. Tiles in the mosaic are spaced by $2.^\circ5$ in each direction. Thus, there are 49 tiles in the mosaic for each active region. Finally, the residual velocity in different regions is calculated by subtracting the velocity in quiet regions at the

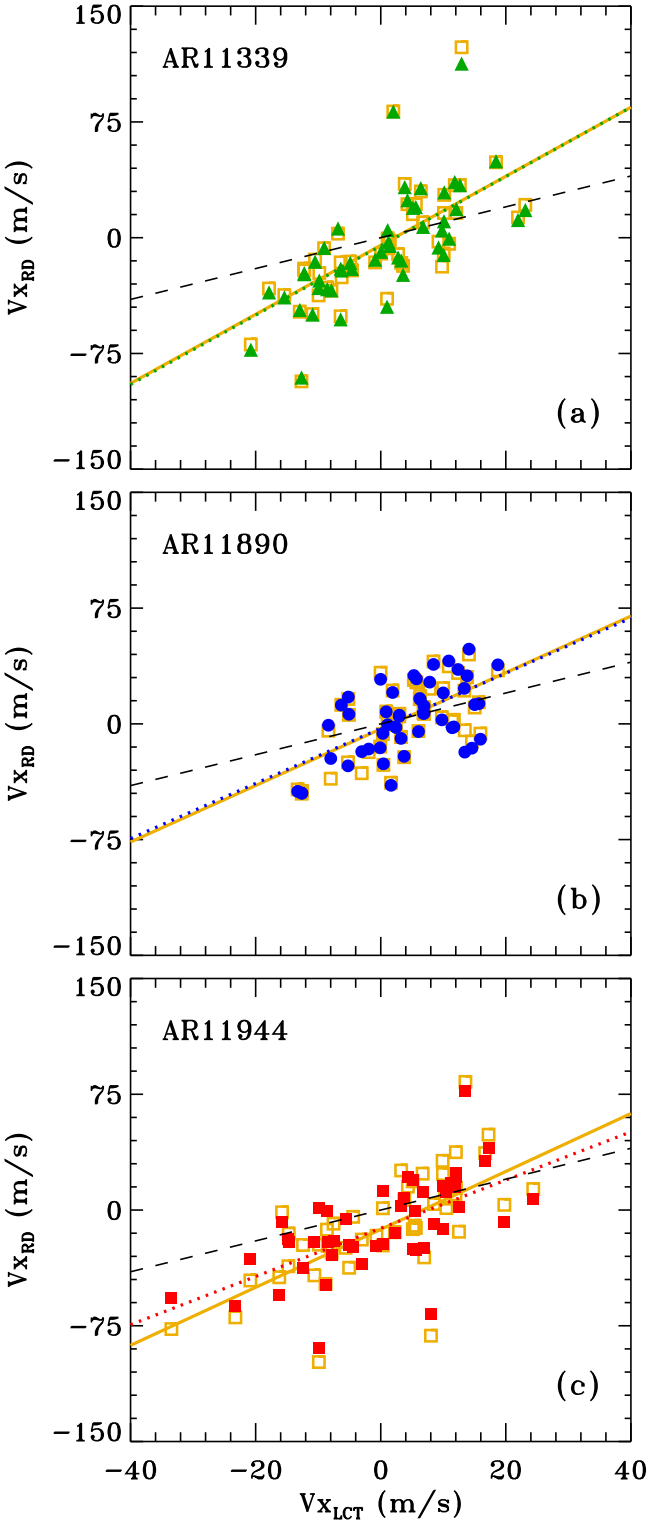


**Figure 5.** Comparison between zonal components of photospheric flows from LCT ($Vx_{\rm LCT}$) and subphotospheric flows near surface from the ring-diagram technique ($Vx_{\rm RD}$) in three active regions: (a) AR 11339, (b) AR 11890, and (c) AR 11944. Subphotospheric flows calculated using velocities of fitted $f$ modes are shown by open yellow squares, while inverted flows are shown by the filled symbols, and their linear fits are shown by solid and dotted lines, respectively. Dashed lines represent the ideal scenario for both velocities $Vx_{\rm LCT}$ and $Vx_{\rm RD}$. Uncertainties in velocity estimation are smaller than the size of symbols.

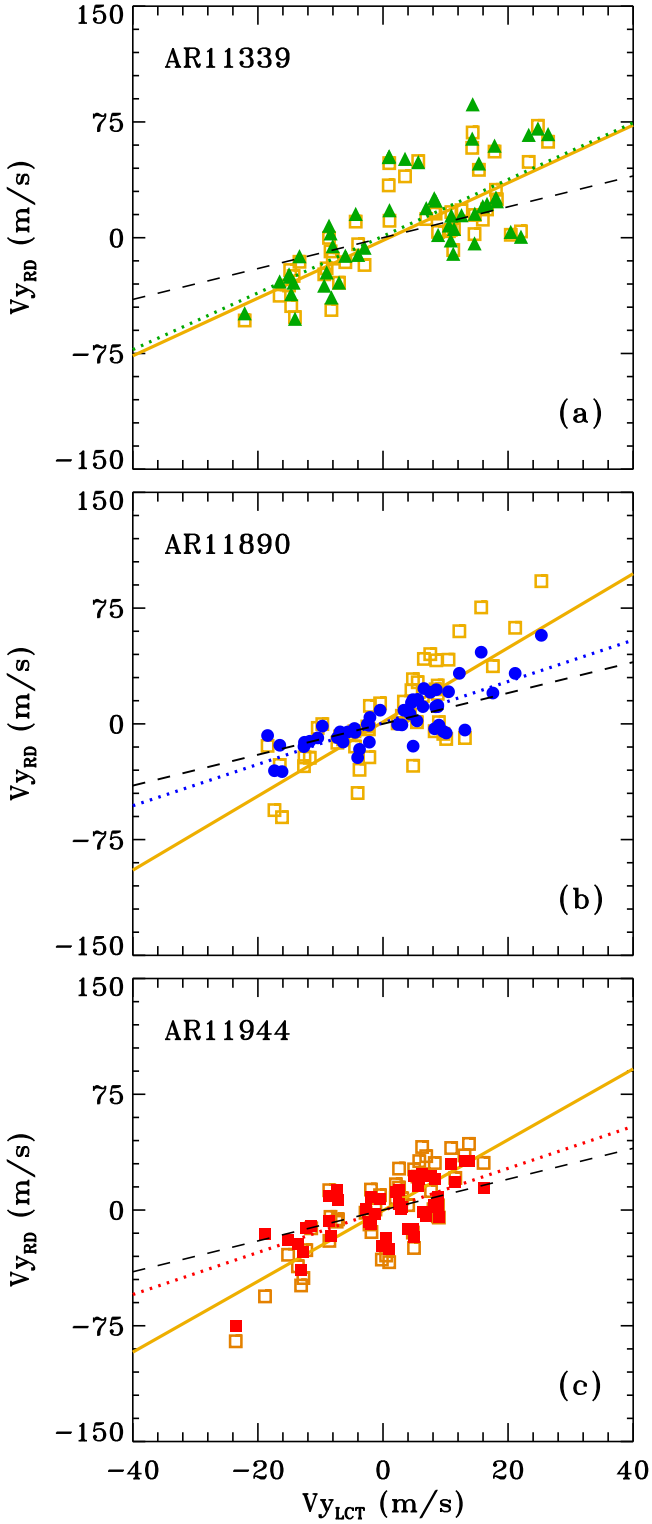


**Figure 6.** Comparison between meridional components of photospheric flows from LCT ($Vy_{\rm LCT}$) and subphotospheric flows near the surface from the ring-diagram technique ($Vy_{\rm RD}$) in three active regions: (a) AR 11339, (b) AR 11890, and (c) AR 11944. Subphotospheric flows calculated using velocities of fitted $f$ modes are shown by open yellow squares, while inverted flows are shown by the filled symbols, and their linear fits are shown by solid and dotted lines, respectively. Dashed lines represent the ideal scenario for both velocities $Vy_{\rm LCT}$ and $Vy_{\rm RD}$. Uncertainties in velocity estimation are smaller than the size of symbols.

**Table 2**
Statistical Analysis between Flows from Local Correlation Tracking (LCT) and Ring-diagram (RD) Methods

| AR | RD | Zonal | | | | Meridional | | | |
|---|---|---|---|---|---|---|---|---|---|
| Number | Flow[a] | $r_P$ | $r_S$ | $P_S$ | Slope[b] | $r_P$ | $r_S$ | $P_S$ | Slope[b] |
| 11339 | Fit | 0.69 | 0.79 | $10^{-11}$ | $2.24 \pm 0.03$ | 0.78 | 0.77 | $10^{-11}$ | $1.87 \pm 0.02$ |
| | Inv | 0.71 | 0.82 | $10^{-13}$ | $2.25 \pm 0.04$ | 0.73 | 0.73 | $10^{-09}$ | $1.84 \pm 0.03$ |
| 11890 | Fit | 0.62 | 0.54 | $10^{-06}$ | $1.83 \pm 0.04$ | 0.78 | 0.74 | $10^{-09}$ | $2.51 \pm 0.03$ |
| | Inv | 0.58 | 0.51 | $10^{-05}$ | $1.79 \pm 0.04$ | 0.79 | 0.75 | $10^{-10}$ | $1.34 \pm 0.03$ |
| 11944 | Fit | 0.69 | 0.74 | $10^{-09}$ | $1.88 \pm 0.02$ | 0.79 | 0.73 | $10^{-09}$ | $2.29 \pm 0.04$ |
| | Inv | 0.65 | 0.67 | $10^{-07}$ | $1.56 \pm 0.03$ | 0.71 | 0.66 | $10^{-07}$ | $1.36 \pm 0.03$ |
| All | Fit | 0.68 | 0.73 | $10^{-25}$ | $2.01 \pm 0.02$ | 0.78 | 0.76 | $10^{-28}$ | $2.11 \pm 0.02$ |
| | Inv | 0.66 | 0.70 | $10^{-22}$ | $1.87 \pm 0.02$ | 0.74 | 0.74 | $10^{-26}$ | $1.51 \pm 0.02$ |

**Notes.**
[a] Type of RD method to calculate flows.
[b] Slopes are calculated by performing the least-squares fits between LCT and RD velocities; the errors in LCT are considered to be zero, while in RD these are the statistical uncertainties.

same heliographic location in a nearby Carrington rotation as discussed in Jain et al. (2012, 2015).

## 3. ANALYSIS AND RESULTS

### 3.1. Flows from RD Method

We obtain two types of velocities in the RD method: fitted and inverted. In the best scenario, the fitted velocity should be comparable to the inverted velocity when proper depth range is taken into account. In order to infer velocity in the near-surface shear layer for comparison with the photospheric values, we compute velocities from both methods: (i) calculate velocity residuals of zonal and meridional components of the fitted velocity of surface gravity waves (*f*-modes) only, and (ii) calculate velocity residuals of inverted velocities in the upper 2 Mm. Note that the surface gravity waves only provide direct measurement of flow velocity in the layers where *f* modes have significant amplitude, i.e., the layer spanning about 2 Mm below the surface. This approach has been exploited by several authors in RD analysis, for example, Hindman et al. (2009) studied flows in smaller regions of filaments, and more recently Bogart et al. (2015) investigated typical structures associated with magnetic belts and regions of magnetic activity in the outer 1% of the Sun. Moreover, the *f*-mode ridges have also been isolated to construct travel-time maps near the surface in the TD technique (Georgobiani et al. 2007). In Figure 3, we demonstrate the direct comparison between fitted and inverted velocities. Here we show scatter plots of four quantities, i.e., $V_x$, $V_y$, total magnitude ($|V_{\rm Total}| = (V_x^2 + V_y^2)^{1/2}$), and the azimuthal angle ($\theta$) of the horizontal velocity. In all cases, we show the ideal scenarios by the dotted lines, where fitted and inverted values should be in agreement.

We statistically test the correspondence between both methods by calculating Pearson ($r_P$) and Spearman ($r_S$) correlation coefficients. While $r_P$ is used to measure the linear association between two variables, $r_S$ measures the extent of association that may exist between two series of ranks for the same set of variables. The linear correlation is calculated using the following expression:

$$r_P = \frac{\sum_i u_i v_i}{\left(\sum_i |u_i|^2 \sum_i |v_i|^2\right)^{1/2}}, \quad (2)$$

where $u_i$ and $v_i$ are two scalar variables. When there are no tied ranks in either column of data, the $r_S$ can be simplified to

$$r_S = 1 - \frac{6\sum_{i=1}^{n} d_i^2}{n^3 - n}, \quad (3)$$

where $d_i$ is the difference between ranks for observation $i$ and $n$ is the sample size.

We find a good agreement between fitted and inverted values. The calculated values of $r_P$ for $V_x$, $V_y$, $|V_{\rm Total}|$, and $\theta$ are 0.99, 0.98, 0.91, and 0.87, respectively, while corresponding $r_S$ are 0.98, 0.99, 0.84, and 0.97. It is also noticed that the individual components from two approaches are better correlated than the total magnitude and azimuthal angle. We further notice that the fitted zonal and meridional components for AR 11339 are much closer to the inverted values as compared to the other two active regions. The maximum deviation is seen in the meridional component of AR 11890, where fitted values are higher than those obtained from inversion.

### 3.2. Flows from LCT Method

We show, in Figure 4, the maps of zonal and meridional components of horizontal velocity at the surface for each active region using the LCT method. These maps display values between +30 and −30 m s$^{-1}$ in general, except for some areas of higher values. A closer examination of these maps with Figure 1 clearly indicates that the higher values are obtained at the locations of sunspots. We also include the maps of magnitude (third row from the top) and the direction (bottom row) of total horizontal velocity in the same figure. In these maps, we find an excess velocity in penumbrae of large sunspots. We also obtain an outflow in penumbrae and the inflow in umbrae of all major sunspots in active regions. These findings are in agreement with earlier results.

### 3.3. Comparison between Flows from RD and LCT Methods: Zonal and Meridional Components

As discussed earlier, the flows from LCT and RD methods are generally calculated at two different spatial scales. While LCT is able to track changes in velocity fields of small elements on the surface, the RD method provides estimates of average velocity only for regions that are much bigger in size. In order to examine the similarities/dissimilarities between

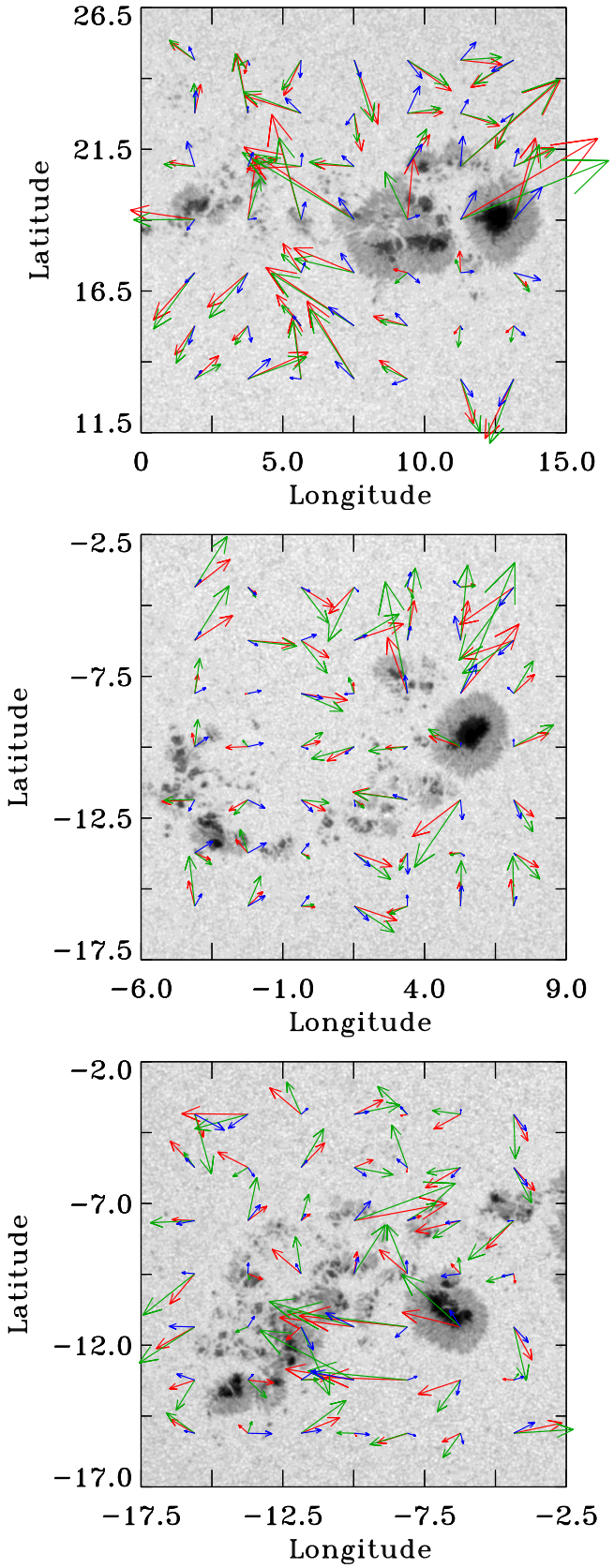


**Figure 7.** Comparison of horizontal flows: photospheric from LCT (blue), subphotospheric from *f*-modes (green), and subphotospheric inverted velocities (red) in AR 11339 (top), AR 11890 (middle), and AR 11944 (bottom).

**Table 3**
Merit Analysis of Total Horizontal Velocity

| Velocity Vectors | Metrics of Merit | AR 11339 | AR 11890 | AR 11944 | All |
|---|---|---|---|---|---|
| $V_{LCT}$ and $V_{Fit}$ | $r_P$ | 0.55 | 0.43 | 0.54 | 0.53 |
| | $C_{vec}$ | 0.73 | 0.72 | 0.71 | 0.72 |
| | $C_{CS}$ | 0.72 | 0.67 | 0.65 | 0.67 |
| $V_{LCT}$ and $V_{Inv}$ | $r_P$ | 0.50 | 0.43 | 0.46 | 0.47 |
| | $C_{vec}$ | 0.72 | 0.66 | 0.64 | 0.69 |
| | $C_{CS}$ | 0.71 | 0.61 | 0.60 | 0.62 |

them, the velocity components from LCT have been averaged over the same grid as in the RD method. This allows us to perform one-to-one comparison between flows from both methods. Figures 5 and 6 exhibit scatter plots of *x*- and *y*-components from the LCT method versus those obtained from both approaches of the RD method. We notice a visible difference in their magnitudes: the values obtained from the RD method are larger than those from the LCT method. The solid and dotted lines in these figures correspond to the best linear fit between LCT and two values from the RD, while the dashed lines are drawn to depict the same values from all methods. The linear fits are obtained from the least-squares method; the errors in LCT are considered to be zero, while in RD these are the statistical uncertainties in velocity determination.

In order to quantify the similarities and/or differences in computed zonal and meridional components from different methods, we provide results of the statistical analysis in Table 2. In most cases, the correlation coefficients are higher than 0.60. We note that the LCT values are better correlated with the RD fitted values than those from the inversion. Also, the meridional component has higher correlation than the zonal component. This is in contrast to the results from TD analysis, where the zonal component of the flow near surface is found to be better correlated with the surface measurements (Švanda et al. 2007; Liu et al. 2013). We also compute slopes of the best-fitted lines for individual active regions and by combining all data points together. The slopes differ significantly from the ideal value of 1.0. However, we also obtain similar slopes for both fitted and inverted values for AR 11339. This is similar to the results shown in Figure 3, where both approaches from RD for AR 11339 yield similar values. We further interpret these slopes as the scaling factors between the RD and LCT values. In general, fitted values have higher slopes than the inverted values, indicating larger deviation from the LCT values and also higher correlation coefficients. Quantitatively, both zonal and meridional components in LCT are smaller by a factor of 2 as compared to the fitted velocities and by a factor of 1.8 and 1.5 against inverted zonal and meridional velocities, respectively.

### *3.4. Comparison between Total Horizontal Flows from RD and LCT Methods*

We display in Figure 7 the total horizontal velocity for all three active regions. In addition to the magnitudes, here we also compare the directions of velocity vectors. In order to understand the variation in velocity vectors from region to

region, we overplot these vectors on the HMI continuum images. We find that the large values are obtained for tiles in the vicinity of big sunspots that host the reservoir of strong magnetic fields. A visual inspection of these plots hints at the agreement between different methods, although the magnitudes from LCT are significantly smaller than the RD values. Major discrepancies in the direction are found for tiles with large sunspots; however, there are only a very few tiles where flows from both methods point to the different directions. A detailed quantative study is needed to investigate the correlation between the differences in direction using a large database of active regions and also by including the inclination angle determined from the vector magnetic field data.

We further quantify the degree of agreement in these vectors by analyzing their local characteristics, i.e., the vector magnitude and direction at each grid point. We use all three total horizontal velocity vectors, i.e., $V_{\rm Fit}$, $V_{\rm Inv}$, and $V_{\rm LCT}$, and compute the vector correlation coefficient ($C_{\rm vec}$) and the Cauchy–Schwarz inequality ($C_{\rm CS}$) as described below:

$$C_{\rm vec} = \frac{\sum_i \boldsymbol{U}_i \cdot \boldsymbol{V}_i}{\left(\sum_i |\boldsymbol{U}_i|^2 \sum_i |\boldsymbol{V}_i|^2\right)^{1/2}}, \quad (4)$$

$$C_{\rm CS} = \frac{1}{M}\sum_i \frac{\boldsymbol{U}_i \cdot \boldsymbol{V}_i}{|\boldsymbol{U}_i||\boldsymbol{V}_i|} = \frac{1}{M}\sum_i \cos\theta_i, \quad (5)$$

where $\boldsymbol{U}_i$ and $\boldsymbol{V}_i$ are two velocity vectors, $\theta_i$ the angle between them, and $M$ the total number of vectors. The $C_{\rm vec}$ is equivalent to the correlation coefficients for scalar functions but for the vector quantities, while the $C_{\rm CS}$ is a measure of the angular difference between two vector fields; it is 1 when the fields are parallel and $-1$ for antiparallel fields. Computed $C_{\rm vec}$ and $C_{\rm CS}$ are listed in Table 3, where $r_{\rm P}$ coefficients are also included for comparison. We find higher values for $C_{\rm vec}$ as compared to $r_{\rm P}$. Obtained positive higher values of $C_{\rm CS}$ also indicate that these velocity vectors point in the same direction. We again find better agreement between LCT and fitted velocities over the LCT and inverted velocities. This might be due to the way these quantities are computed as the inversion is performed on the fitted velocities, which may add another set of uncertainties to the inverted velocities. Although due to the limitations on spatial scale in the RD method, we cannot compute flows confined to penumbral and umbral regions separately; a close correspondence between LCT and RD methods clearly implies that similar flows are inferred from both the methods in these areas.

## 4. SUMMARY

We have measured zonal and meridional components of the horizontal velocity near the surface in three active regions. Velocities in the upper 2 Mm of the subphotospheric layer are calculated using the RD technique of helioseismology, while the LCT of surface features is applied to estimate flows in the photosphere. Although both methods employ different spatial scales, we find positive and significant correlation between the individual components of the flows. This clearly indicates that despite the absorption of acoustic power in active regions, the overall trends in flows calculated from the helioseismology are comparable to the surface measurements. However, the magnitudes of velocity in both methods are significantly different. The velocity from the LCT method is smaller by a factor of 2 (as a consequence of averaging), and the median difference between the direction of corresponding vectors is 49°. Further, the magnitudes of fitted and inverted velocities from the RD method are comparable, implying that the inversion technique used in the RD analysis (RLS in this case) provides reliable estimates of the inferred flows.

*SDO* data courtesy of *SDO* (NASA) and the HMI and AIA consortium. This work was partially supported by NASA grant NNH12AT11I and NSF Award 1062054 to the National Solar Observatory. The ring-diagram analysis was carried out using the NSO/GONG ring-diagram pipeline. This work was performed under the auspices of the SPACEINN Framework of the European Union (EU FP7).

## REFERENCES

Antia, H. M., & Basu, S. 2007, AN, 328, 257
Bogart, R. S., Baldner, C. S., & Basu, S. 2015, ApJ, 807, 125
Duvall, T. L., Jr., Jefferies, S. M., Harvey, J. W., & Pomerantz, M. A. 1993, Natur, 362, 430
Georgobiani, D., Zhao, J., Kosovichev, A. G., et al. 2007, ApJ, 657, 1157
González Hernández, I., Komm, R., Hill, F., et al. 2006, ApJ, 638, 576
Haber, D. A., Hindman, B. W., Toomre, J., et al. 2000, SoPh, 192, 335
Hill, F. 1988, ApJ, 333, 996
Hindman, B. W., Gizon, L., Duvall, T. L., Jr., Haber, D. A., & Toomre, J. 2004, ApJ, 613, 1253
Hindman, B. W., Haber, D. A., & Toomre, J. 2009, ApJ, 698, 1749
Jain, K., Hill, F., Tripathy, S. C., et al. 2008, in ASP Conf. Ser. 383, Subsurface and Atmospheric Influences on Solar Activity, ed. R. Howe et al. (San Francisco, CA: ASP), 389
Jain, K., Komm, R. W., González Hernández, I., Tripathy, S. C., & Hill, F. 2012, SoPh, 279, 349
Jain, K., Tripathy, S. C., & Hill, F. 2009, ApJ, 695, 1567
Jain, K., Tripathy, S. C., & Hill, F. 2015, ApJ, 808, 60
Kholikov, S., & Hill, F. 2014, SoPh, 289, 1077
Komm, R., González Hernández, I., Howe, R., & Hill, F. 2015, SoPh, 290, 1081
Liu, Y., Zhao, J., & Schuck, P. W. 2013, SoPh, 287, 279
November, L. J., & Simon, G. W. 1988, ApJ, 333, 427
Pesnell, W. D., Thompson, B. J., & Chamberlin, P. C. 2012, SoPh, 275, 3
Rajaguru, S. P., Basu, S., & Antia, H. M. 2001, ApJ, 563, 410
Ravindra, B., Longcope, D. W., & Abbett, W. P. 2008, ApJ, 677, 751
Scherrer, P. H., Schou, J., Bush, R. I., et al. 2012, SoPh, 275, 207
Snodgrass, H. B. 1984, SoPh, 94, 13
Švanda, M., Roudier, T., Rieutord, M., Burston, R., & Gizon, L. 2013, ApJ, 771, 32
Švanda, M., Zhao, J., & Kosovichev, A. G. 2007, SoPh, 241, 27
Zhao, J., Bogart, R. S., Kosovichev, A. G., Duvall, T. L., Jr., & Hartlep, T. 2013, ApJL, 774, L29
Zhao, J., Georgobiani, D., Kosovichev, A. G., et al. 2007, ApJ, 659, 848